Adaptive numerical solution of thick plates using first-order shear deformation theory. Part II: Adaptivity.

M.J. Ludwig[1], Simon Shaw and J.R. Whiteman
Department of Mathematics and Statistics,
Brunel University, Uxbridge, Middlesex, UB8 3PH U.K.

This is the second in a pair of papers concerned with the adaptive finite element solution of Riessner-Mindlin thick plates modelled using first order shear deformation theory. This paper is concerned with enhancing the *a posteriori* energy-error estimators developed in Part I in order to accomodate transition elements in the finite element mesh. The resulting estimators are then used in an adaptive finite element model employing transition elements and the subsequent results discussed and compared with those in Part I. A major part of the paper is devoted to identifying a novel patch assembly node algorithm for using the ZZ recovery-type estimator with transition elements. © (Year) John Wiley & Sons, Inc.

Keywords: adaptivity, transition elements, thick plates, first order shear deformation.

I. INTRODUCTION

This is Part II of a pair of papers concerned with the adaptive finite element solution of Riessner-Mindlin thick plates modelled using first order shear deformation theory (FSDT). In Part I [9] we described the problem and gave a finite element formulation based on bilinear elements. We then derived *a posteriori* error estimates of both the residual and recovery types, and tested them on uniformly refined meshes on a square domain Ω. In this article we use these estimates in adaptive schemes making use of transition elements.

The remainder of this section is concerned with a brief re-cap of the problem and a short introduction to the concept of a transition element.

In the next section, Section II., we detail the modifications required to the JH-P residual estimator of Johnson-Hansbo type (see [7]). This involves identifying derivative

[1]Ludwig would like to acknowledge the support of a research studentship from the Engineering and Physical Sciences Research Council

© (Year) John Wiley & Sons, Inc. CCC (cccline information)

discontinuities *inside* the elements and allowing for them when forming the residual. It also requires new interpolation-error constants.

In Section III. we investigate the Zinkiewicz-Zhu estimator for plates, ZZ-P, with a particular regard to identifying a sampling strategy for the stresses. It is believed that these are the first such results for transition elements, and because of this we include full details of the patch assembly node algorithm.

The adaptive strategies are put to work in Section IV. on test problems and the paper finishes with some thought on how the estimators may be improved further in Section V..

We are concerned with thick plates modelled using first-order shear deformation theory as described by Reddy, [12]. To recap, the term first order arises due to the order of approximation of the three global displacements u_1, u_2 and u_3. The approximation is written in power series of the thickness coordinate and unknown functions in the following way,

$$\begin{aligned} u_1(x_1,x_2,x_3) &= u(x_1,x_2) + x_3\psi_1(x_1,x_2), \\ u_2(x_1,x_2,x_3) &= v(x_1,x_2) + x_3\psi_2(x_1,x_2), \\ u_3(x_1,x_2,x_3) &= w(x_1,x_2). \end{aligned} \tag{1.1}$$

The unknowns are the axial displacements u, v and w and the two rotations ψ_1 and ψ_2. By using the usual strain tensor and contracted notations: $\varepsilon_i \equiv \varepsilon_{ii}$ for $i = 1,2,3$; and: also where $\varepsilon_4 \equiv 2\varepsilon_{12}$, $\varepsilon_5 \equiv 2\varepsilon_{13}$ and $\varepsilon_6 \equiv 2\varepsilon_{23}$ it is possible to express the strains for the plate problem as,

$$\varepsilon_i = \varepsilon_i^{(0)} + x_3\varepsilon_i^{(1)} \quad i = 1,2,4,5,6. \tag{1.2}$$

For further details on the model we refer back to [9] and also to [8] but, to summarise, the equilibrium equations for the problem may be expressed in the form,

$$\frac{\partial N_1}{\partial x_1} + \frac{\partial N_4}{\partial x_2} = 0, \tag{1.3}$$

$$\frac{\partial N_4}{\partial x_1} + \frac{\partial N_2}{\partial x_2} = 0, \tag{1.4}$$

$$\frac{\partial Q_5}{\partial x_1} + \frac{\partial Q_6}{\partial x_2} + q = 0, \tag{1.5}$$

$$\frac{\partial M_1}{\partial x_1} + \frac{\partial M_4}{\partial x_2} - Q_5 = 0, \tag{1.6}$$

$$\frac{\partial M_4}{\partial x_1} + \frac{\partial M_2}{\partial x_2} - Q_6 = 0. \tag{1.7}$$

In the above N_i and M_i for $i = 1,2,4$ are known as the stress and bending moment resultants respectively. As described by Ochoa and Reddy, [11], for a laminated plate consisting of $\mathcal{M}$ layers and with each layer located between $x_3 = t_m$ and $x_3 = t_{m+1}$ for $m = 1,\ldots,\mathcal{M}$ and such that $t_1 = -t/2$ and $t_{\mathcal{M}+1} = t/2$,

$$\begin{bmatrix} N_1 \\ N_2 \\ N_4 \end{bmatrix} = \begin{bmatrix} A_{11} & A_{12} & A_{14} \\ A_{12} & A_{22} & A_{24} \\ A_{14} & A_{24} & A_{44} \end{bmatrix} \begin{bmatrix} \varepsilon_1^{(0)} \\ \varepsilon_2^{(0)} \\ \varepsilon_4^{(0)} \end{bmatrix} + \begin{bmatrix} B_{11} & B_{12} & B_{14} \\ B_{12} & B_{22} & B_{24} \\ B_{14} & B_{24} & B_{44} \end{bmatrix} \begin{bmatrix} \varepsilon_1^{(1)} \\ \varepsilon_2^{(1)} \\ \varepsilon_4^{(1)} \end{bmatrix}, \tag{1.8}$$

and,

$$\begin{bmatrix} M_1 \\ M_2 \\ M_4 \end{bmatrix} = \begin{bmatrix} B_{11} & B_{12} & B_{14} \\ B_{12} & B_{22} & B_{24} \\ B_{14} & B_{24} & B_{44} \end{bmatrix} \begin{bmatrix} \varepsilon_1^{(0)} \\ \varepsilon_2^{(0)} \\ \varepsilon_4^{(0)} \end{bmatrix} + \begin{bmatrix} D_{11} & D_{12} & D_{14} \\ D_{12} & D_{22} & D_{24} \\ D_{14} & D_{24} & D_{44} \end{bmatrix} \begin{bmatrix} \varepsilon_1^{(1)} \\ \varepsilon_2^{(1)} \\ \varepsilon_4^{(1)} \end{bmatrix}, \tag{1.9}$$

where Equation (1.2) has been used and where A_{ij}, B_{ij} and D_{ij} for $i, j = 1, 2, 4$ are the in-plane, bending-stretching and bending stiffnesses of the plate respectively and expressed as,

$$(A_{ij}, B_{ij}, D_{ij}) = \sum_{m=1}^{\mathcal{M}} \int_{t_m}^{t_{m+1}} C_{ij}^m \left(1, x_3, x_3^2\right) \, dx_3, \quad i, j = 1, 2, 4. \tag{1.10}$$

In the above it can be seen that the terms in the constitutive matrix $\mathbf{C}^m$ arising from Hooke's law in each layer $m = 1, \ldots, \mathcal{M}$ are integrated and then summed through the thickness of the plate as described in [11]. In addition, the transverse shear force resultants have the form,

$$\begin{bmatrix} Q_5 \\ Q_6 \end{bmatrix} = \begin{bmatrix} A_{55} & A_{56} \\ A_{56} & A_{66} \end{bmatrix} \begin{bmatrix} \varepsilon_5^{(0)} \\ \varepsilon_6^{(0)} \end{bmatrix}, \tag{1.11}$$

where,

$$A_{ij} = K_i K_j \sum_{m=1}^{\mathcal{M}} \int_{t_m}^{t_{m+1}} C_{ij}^m \, dx_3 \quad i, j = 5, 6, \tag{1.12}$$

and where K_i and K_j are shear correction coefficients which, for FSDT are taken to be $K_i^2 = K_j^2 = 5/6$ as also detailed in [11]. Note that in the case of a single layered plate $B_{ij} = 0$ for $i, j = 1, 2, 4$ and the model simplifies considerably. For a description of the boundary condition data see [9].

A. Weak formulation

Rather than duplicate much of the material already present in [9] we just recall the weak form of the problem from Sections III and IV in [9]. The weak problem is to find $\mathbf{u} \in V$ such that,

$$a(\mathbf{u}, \mathbf{v}) = F(\mathbf{v}), \quad \forall\, \mathbf{v} \in V, \tag{1.13}$$

and where V is an appropriate subspace of $\left[H^1(\Omega)\right]^5$ containing the essential boundary conditions. By identifying a suitable finite element subspace $V^h \subset V$, based on quadrilateral transition elements derived from bilinear shape functions, the finite element approximation is then: find $\mathbf{u}_h \in V^h$ such that,

$$a(\mathbf{u}_h, \mathbf{v}_h) = F(\mathbf{v}_h) \quad \forall \quad \mathbf{v}_h \in V^h. \tag{1.14}$$

We now briefly describe the concept of a transition element.

B. Transition elements

The aim of this work is to detail the modifications necessary to the error estimators described in [9] for use in adaptive schemes employing transition elements. As described by Choi and Park, [4], [5] and Gupta [6], these elements can have five, six or seven nodes and provide a transition in the mesh from elements of side length $h = m/2$ to elements of side length $h = m$ for some m. A typical scenario is illustrated in Figure (1) where a transition element (shaded) with an irregular mid-side node on the western edge is used to provide a transition in the mesh from finer elements to coarser ones. For convenience

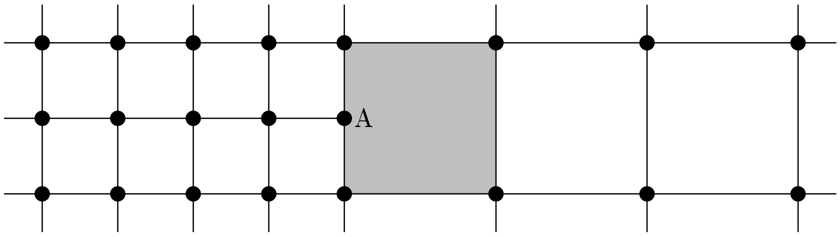

FIG. 1. 1-irregular transition element (shaded).

let this type of transition element be known as a 1-irregular transition element due to the presence of the single irregular node A. Similarly, we call a transition element having six nodes a 2-irregular transition element (there are two kinds of these—we'll return to this point later), and one having seven nodes a 3-irregular transition element. The shape function and quadrature modifications necessary to employ the transition elements in the model are as described by Gupta, [6].

II. JOHNSON-HANSBO TYPE ERROR ESTIMATE FOR PLATES (JH-P)

The residual type estimator, called JH-P, derived in [9] is based on that given for linear elasticity by Johnson and Hansbo in [7]. Essentially it consists of internal residuals on each element formed from the finite element stresses $\mathbf{T}$ and body forces $\mathbf{f}$, and stress jumps across the element boundaries. In this section the modifications required for the application in the adaptive mode are discussed.

As a starting point the error, measured in the energy norm and using the technique of Johnson and Hansbo, [7], can be expressed as described in [9] as,

$$\begin{aligned} \|\mathbf{e}\|^2_{E(\Omega)} &= \sum_{k=1}^{N} \int_{\Omega_k} (\mathbf{f} + \operatorname{div} \mathbf{T}(\mathbf{u}_h) - \mathbf{q}(\mathbf{u}_h)) \cdot (\mathbf{e} - \pi_h \mathbf{e})\, d\mathbf{x} \\ &- \sum_{k=1}^{N} \int_{\partial\Omega_k} (\mathbf{T}(\mathbf{u}_h)\, \mathbf{n}_k) \cdot (\mathbf{e} - \pi_h \mathbf{e})\, ds \\ &+ \int_{\hat{\Gamma}_1} \hat{N}_n (e_1 - \pi_h e_1)\, ds + \int_{\hat{\Gamma}_2} \hat{N}_s (e_2 - \pi_h e_2)\, ds + \int_{\hat{\Gamma}_3} \hat{Q} n (e_3 - \pi_h e_3)\, ds \\ &+ \int_{\hat{\Gamma}_4} \hat{M}_n (e_4 - \pi_h e_4)\, ds + \int_{\hat{\Gamma}_5} \hat{M}_s (e_5 - \pi_h e_5)\, ds, \end{aligned} \tag{2.1}$$

where $\mathbf{f} = (0, 0, q, 0, 0)^T$ is the applied transverse load, $\mathbf{n}_k$ is the unit outward normal to the boundary $\partial\Omega_k$ of element Ω_k and all further notation is as described in [9].

Due to the presence of transition elements in the mesh we consider each element Ω_k to be decomposed into four smaller ones, as shown in Figure (2). We consider Ω_k as a 'composite' element, consisting of four 'sub-element' regions denoted Ω_{kl} for $l = 1, 2, 3$ and 4. This configuration is to allow for the effect of possible lines of slope discontinuity

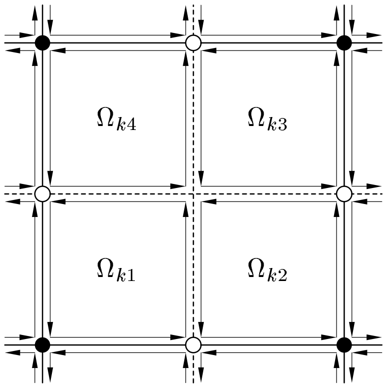

FIG. 2. General element Ω_k depicted as a possible composite of four sub-element regions.

running across the element and included in the figure as broken lines. Such lines arise from the presence of irregular mid-side nodes on the element which are illustrated at their four possible locations by empty circles (the standard corner nodes are illustrated by filled circles). It should be noted at this point that although the recommendation is for all elements to be considered as 'composite' elements, in some cases four sub-element regions are not necessary. Such cases arise whenever the element is not a transition element or when it is a 1-irregular element. In such cases the regions are retained but may or may not have slope discontinuities between them. This will not effect the computations over the element but by considering the most general case we are taking into account the whole transition family along with the standard non-transition element configurations.

The introduction of the sub-element regions in turn introduces modifications to the error representation formula given above. The integration over the elements for example, given in Equation (2.1) as,

$$\sum_{k=1}^{N} \int_{\Omega_k} (\mathbf{f} + \mathrm{div}\mathbf{T}(\mathbf{u}_h) - \mathbf{q}(\mathbf{u}_h)) \cdot (\mathbf{e} - \pi_h \mathbf{e})\, d\mathbf{x}, \tag{2.2}$$

now becomes,

$$\sum_{k=1}^{N} \sum_{l=1}^{4} \int_{\Omega_{kl}} (\mathbf{f} + \mathrm{div}\mathbf{T}(\mathbf{u}_h) - \mathbf{q}(\mathbf{u}_h)) \cdot (\mathbf{e} - \pi_h \mathbf{e})\, d\mathbf{x}, \tag{2.3}$$

which involves an additional summation over the sub-element regions. Integrating over each Ω_k in this piecewise manner can be achieved by implementing a quadrature scheme on each sub-element. The integral can thus still be considered as a sum over all elements Ω_k, noting that, for the case where Ω_k is a transition element, the integration is modified accordingly to cope with the sub-element region features as described by Gupta, [6].

The effect of sub-element regions must now also be considered for the integral around element boundaries. Thus, as in the above modification for the element interior integral, the boundary integral given in Equation (2.1) as,

$$-\sum_{k=1}^{N}\int_{\partial\Omega_k}(\mathbf{T}(\mathbf{u}_h)\,\mathbf{n}_k)\cdot(\mathbf{e}-\pi_h\mathbf{e})\,ds, \tag{2.4}$$

now becomes,

$$-\sum_{k=1}^{N}\sum_{l=1}^{4}\int_{\partial\Omega_{kl}}(\mathbf{T}(\mathbf{u}_h)\,\mathbf{n}_{kl})\cdot(\mathbf{e}-\pi_h\mathbf{e})\,ds, \tag{2.5}$$

where $\mathbf{n}_{kl}$ denotes the unit outward normal to the boundary $\partial\Omega_{kl}$ of sub-element region Ω_{kl} spawned from 'parent' element Ω_k.

Considering the integration around each perimeter $\partial\Omega_{kl}$ as illustrated in Figure (2) it is clear that integration will be performed twice along each element edge $s \in (\partial\Omega_k \cap \partial\Omega_{kl}) \setminus \partial\Omega \equiv S_k$ where $\cup_k S_k \equiv S$ which is the set of internal element edges used in [9]. In addition, integration will also be performed twice along each edge $t \in \partial\Omega_{kl} \setminus \partial\Omega_k \equiv T_k$ which coincides with the interior lines of slope discontinuity in the element Ω_k and where $\cup_k T_k \equiv T$. Here we have used the terms 'internal' and 'interior', the meanings of these are not the same. We shall use the term 'internal' when describing element edges which are internal as far as the problem domain is concerned. These are true element edges and belong to set S. The term 'interior' will be used to describe the interior features of a transition element, thus a 1-irregular element will have one interior line of possible slope discontinuity which belongs to set T. It was seen in [9] that integration around the element boundaries produced stress jumps across common internal element edges. These jumps will again arise here and for the case of transition elements additional 'interior' stress jumps will arise.

The addition of the transition element effects enable the error estimate to be expressed again as,

$$||\mathbf{e}||^2_{E(\Omega)} = E_1 + E_2,$$

where now, however,

$$E_1 \equiv \sum_{k=1}^{N}\sum_{l=1}^{4}\int_{\Omega_{kl}}\mathcal{R}_1(\mathbf{u}_h)\cdot(\mathbf{e}-\pi_h\mathbf{e})\,d\mathbf{x}, \tag{2.6}$$

and,

$$E_2 \equiv \sum_{k=1}^{N}\sum_{l=1}^{4}\int_{\partial\Omega_{kl}}h_k\mathcal{R}_2(\mathbf{u}_h)\cdot(\mathbf{e}-\pi_h\mathbf{e})\,ds, \tag{2.7}$$

with,

$$\mathcal{R}_1(\mathbf{u}_h) = \mathbf{f} + \operatorname{div}\mathbf{T}(\mathbf{u}_h) - \mathbf{q}(\mathbf{u}_h), \text{ on } \Omega_{kl}, \tag{2.8}$$

and,

$$\mathcal{R}_2(\mathbf{u}_h) = \begin{cases} \frac{1}{2h_k}\left[\mathbf{T}(\mathbf{u}_h)\mathbf{n}_s\right], & \text{on } s \in S_k \text{ for each } \Omega_k, \\ \frac{1}{h_k}\left[\mathbf{T}(\mathbf{u}_h)\mathbf{n}_s\right], & \text{on } t \in T_k \text{ for each } \Omega_k, \\ \frac{1}{h_k}\left[\hat{N}_n - N_n^h, 0, 0, 0, 0\right]^T, & \text{on } \partial\Omega_{kl} \cap \hat{\Gamma}_1, \\ \frac{1}{h_k}\left[0, \hat{N}_s - N_s^h, 0, 0, 0\right]^T, & \text{on } \partial\Omega_{kl} \cap \hat{\Gamma}_2, \\ \frac{1}{h_k}\left[0, 0, \hat{Q}_n - Q_n^h, 0, 0\right]^T, & \text{on } \partial\Omega_{kl} \cap \hat{\Gamma}_3, \\ \frac{1}{h_k}\left[0, 0, 0, \hat{M}_n - M_n^h, 0\right]^T, & \text{on } \partial\Omega_{kl} \cap \hat{\Gamma}_4, \\ \frac{1}{h_k}\left[0, 0, 0, 0, \hat{M}_s - M_s^h\right]^T, & \text{on } \partial\Omega_{kl} \cap \hat{\Gamma}_5, \end{cases} \tag{2.9}$$

where $\mathbf{f} = [0, 0, q, 0, 0]^T$ for an applied transverse load, $\mathbf{q}(\mathbf{u}_h) = \left[0, 0, 0, Q_5^h, Q_6^h\right]^T$ and the jump terms are as described in [9].

The interpolation error bounds given in [9] may now be expressed for a typical element Ω_k and taking into account the possible sub-element regions as,

$$\left[\sum_{l=1}^{4} \|\mathbf{e} - \pi_h \mathbf{e}\|^2_{L_2(\Omega_{kl})}\right]^{\frac{1}{2}} \leq C^i_{1,k} h_k \|\mathbf{e}\|_{E(\Omega_k)}, \tag{2.10}$$

and,

$$\left[\sum_{l=1}^{4} \|\mathbf{e} - \pi_h \mathbf{e}\|^2_{L_2(\partial\Omega_{kl})}\right]^{\frac{1}{2}} \leq C^i_{2,k} h_k^{\frac{1}{2}} \|\mathbf{e}\|_{E(\Omega_k)}. \tag{2.11}$$

Where now,

$$C^i_{1,k} = \sup_{\boldsymbol{\tau} \in \hat{V}} \frac{h_k^{-1}\left[\sum_{l=1}^{4} \|\boldsymbol{\tau} - \pi_h \boldsymbol{\tau}\|^2_{L_2(\Omega_{kl})}\right]^{\frac{1}{2}}}{\|\boldsymbol{\tau}\|_{E(\Omega_k)}}, \tag{2.12}$$

and,

$$C^i_{2,k} = \sup_{\boldsymbol{\tau} \in \hat{V}} \frac{h_k^{\frac{1}{2}}\left[\sum_{l=1}^{4} \|\boldsymbol{\tau} - \pi_h \boldsymbol{\tau}\|^2_{L_2(\partial\Omega_{kl})}\right]^{\frac{1}{2}}}{\|\boldsymbol{\tau}\|_{E(\Omega_k)}}, \tag{2.13}$$

where $\hat{V} := [H^{1+\epsilon}(\Omega_k)]^5$ (see [8, 9] for details.)

Using the same techniques as described in [9] the error can now be bounded above as,

$$\begin{aligned} \|\mathbf{e}\|_{E(\Omega)} \leq & \left[\sum_{k=1}^{N}\sum_{l=1}^{4}\left[C^i_{1,k} h_k \|\mathcal{R}_1(\mathbf{u}_h)\|_{L_2(\Omega_{kl})}\right]^2\right]^{\frac{1}{2}} \\ & + \left[\sum_{k=1}^{N}\sum_{l=1}^{4}\left[C^i_{2,k} h_k^{\frac{1}{2}} \|h_k \mathcal{R}_2(\mathbf{u}_h)\|_{L_2(\partial\Omega_{kl})}\right]^2\right]^{\frac{1}{2}}. \end{aligned} \tag{2.14}$$

Clearly, for the case where there are no transition elements the estimator will reduce to that of [9] since there will be no interior jumps on the elements and the sub-element region considerations will not be necessary. In order to be able to implement this error estimator, the immediate task is to obtain the interpolation error constants $C^i_{1,k}$ and $C^i_{2,k}$. The technique for doing this will follow the same general scheme described in [9] but applied now to the transition element family.

A. Interpolation error constant calculation

The computation of the interpolation error constants for the transition element family varies little from that described in [9]. Upon comparison of Equations (2.12) and (2.13) above and Equation (6.17) and (6.18) of [9] it can be seen that the only changes to be considered are in the numerator. This difference arises due to the possible presence of the irregular nodes on the transition elements which in turn produce the lines of slope discontinuity.

For the computation of the interior interpolation error constant, $C^i_{1,k}$, the possible presence of the irregular nodes and lines of slope discontinuity can be dealt with by considering the element as portrayed in Figure (2), and using the modified integration of Gupta, [6].

For the computation of the boundary interpolation error constant, $C^i_{2,k}$, the technique is modified slightly. It was shown in [9] that such terms arose from the consideration of inter-element 'jumps' across shared element edges. In the case of transition elements we not only have to consider the inter-element jumps, but also the possibility of interior jumps along the broken lines shown in part (b) of Figure (3). Thus it is required that

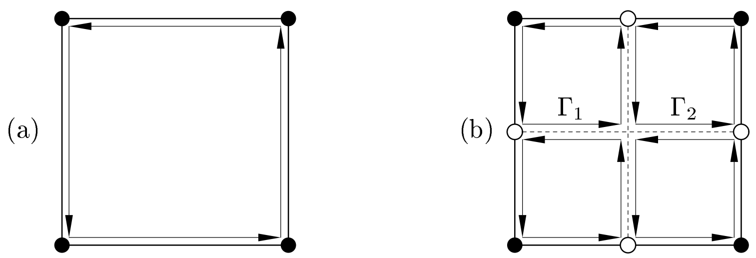

FIG. 3. Integration routes for C^i_2 computation for (a) bilinear interpolant and (b) transition element interpolant.

for all elements the integration is performed not only around the element boundary (illustrated in part (a) of Figure (3)) but also along the internal lines of possible slope discontinuity. It should be noted that for transition elements which only have one line of slope discontinuity, the integrals across the element interior which do not follow a line of slope discontinuity sum to zero. Thus for the 1-irregular northern element with line of slope discontinuity running from North to South face, integration along Γ_1 and Γ_2 portions in Figure (3) will sum to zero and thus have no effect upon the computed value of C^i_2. This is also the case for the standard bilinear interpolant where there are no lines of slope discontinuity and the resulting value for C^i_2 will be identical whether the integration route of (a) or (b) is used. Results for the interpolation error constant values for the transition element family are shown later in Table (V).

III. ZIENKIEWICZ-ZHU TYPE ERROR ESTIMATE FOR PLATES (ZZ-P)

In [9] we termed the ZZ recovery-based error estimate "ZZ-P". In this section we examine the superconvergence properties of the transition elements and derive an adaptive algorithm based on this estimator.

The ZZ-P estimator for use over adapted meshes must be modified in one key area. This involves the selection of the patches of elements around the nodes of interest for which recovery is required. The recovery process as described in [15] in turn relies upon the sampling points used in the element patch. As mentioned in [15] it is desirable for these points to be 'superconvergent' points. These are points at which the normal rate of theoretical convergence is exceeded by one order. The location of such points has been the subject of much investigation following the pioneering work of Barlow [3], which led to the idea of 'Barlow points'. These are highlighted by Ochoa and Reddy, [11], and Reddy and Miravete, [13], for the use in sampling optimal stresses.

Attention here will be focused on research by Mackinnon and Carey, [10], which highlights a particularly appealing approach for predicting the locations of superconvergent points on a typical element. Such analysis is based on the use of Taylor series expansions and developed to determine accuracy estimates for derivatives in one and two dimensions computed by differentiation of a finite element interpolant or approximation. Although research has been performed on standard elements by the authors mentioned in the previous paragraph, the present literature does not contain superconvergent point location predictions for the general transition element. The use of such elements is central to this work and thus the task here is to investigate the transition element family in order to determine whether such points exist and, if so, to calculate their location.

A. Standard element

The analysis will now be performed on the quadrilateral reference element with bilinear shape functions. Such an element has side lengths h, has four nodes and is centered on the origin. The optimal sampling points are well known for the this element and [15], for example, states that such a point resides at the element centroid. This result will now be verified before extending the investigation to problems in the transition element family. In the usual way the value of the interpolant $\pi_h u(\mathbf{x})$ to $u(\mathbf{x})$ at any point $\mathbf{x}$ in the element may be expressed as,

$$\pi_h u(\mathbf{x}) = \sum_{i=1}^{4} u(\mathbf{x}_i)\phi_i(\mathbf{x}) \equiv \sum_{i=1}^{4} u_i\phi_i.$$

Here the $\{\mathbf{x}_i\}$ are the corner node locations. It follows that the derivative with respect to $j = x$ or y, where $\mathbf{x} \equiv (x, y)^T \in \mathbb{R}^2$, can thus be expressed as,

$$\frac{\partial \pi_h u(\mathbf{x})}{\partial j} = \sum_{i=1}^{4} u_i \frac{\partial \phi_i(\mathbf{x})}{\partial j} \equiv \sum_{i=1}^{4} u_i \varphi_i^j,$$

where now the notation, $\varphi_i^j \equiv \partial\phi_i(\mathbf{x})/\partial j$ for $j = x$ or y has been used. Using the notation $\delta_i^j \equiv (j_i - j)$ for $j = x$ or y, the Taylor series expansion of $u(x_i, y_i)$ about a general point (x, y) in the element is given by,

$$u(x_i, y_i) \equiv u_i = u + \delta_i^x u_x + \delta_i^y u_y + \frac{1}{2!}\left[(\delta_i^x)^2 u_{xx} + 2\delta_i^x\delta_i^y u_{xy} + (\delta_i^y)^2 u_{yy}\right]$$

$$+ \frac{1}{3!}\left[\left(\delta_i^x\right)^3 u_{xxx} + 3\left(\delta_i^x\right)^2 \delta_i^y u_{xxy} + 3\delta_i^x \left(\delta_i^y\right)^2 u_{xyy} + \left(\delta_i^y\right)^3 u_{yyy}\right]$$
$$+ \ldots \tag{3.1}$$

for $i = 1, 2, 3$ or 4. Multiplying Equation (3.1) by φ_i^x, summing each term over the nodes, rearranging for the x derivative, and evaluating the summations yields,

$$u_x = \sum_{i=1}^{4} \varphi_i^x u_i + x u_{xx} - \left(\frac{h^2}{24} + \frac{x^2}{2}\right) u_{xxx} - \frac{1}{8}\left(h^2 - 4y^2\right) u_{xyy} + \mathrm{O}(h^3).$$

It can be seen that along the line $x = 0$ the above summation will be an $\mathrm{O}(h^2)$ approximation to u_x. The line $x = 0$ passes through the element centroid and is coincident with the y-axis on the reference element studied, this is often referred to as a 'Gauss line'.

As work is being performed in two dimensions it is natural now to consider the y derivative. The methodology is as above but now Equation (3.1) is multiplied by φ_i^y and each term summed. Upon rearranging and evaluation of the summations the y derivative is given as,

$$u_y = \sum_{i=1}^{4} \varphi_i^y u_i + y u_{yy} - \frac{1}{8}\left(h^2 - 4x^2\right) u_{xxy} - \left(\frac{h^2}{24} + \frac{x^2}{2}\right) u_{yyy} + \mathrm{O}(h^3).$$

In this case it can be seen that along the line $y = 0$ the above summation is in fact an $\mathrm{O}(h^2)$ approximation to the derivative u_y.

Thus, on the reference element, the lines $x = 0$ and $y = 0$ denote superconvergent sampling points for u_x and u_y respectively. It follows therefore that $\nabla \mathbf{u}$ is superconvergent at the origin. This agrees with [9].

B. 1-irregular Element

We begin the analysis of the transition elements with the 1-irregular element with additional Northern node as illustrated in Figure (4). Due to the presence of the irregular node on the North edge of the element there exists the possibility of a slope discontinuity in the derivative of the interpolant across the line $x = 0$. In order to combat this, we consider the element as consisting of two zones. Figure (4) illustrates the choice of zones 1 and 2. The choice of these zones is such that we will be able to give the $|x|$ terms in the element shape functions definite values. Thus, in zone 1, inspection of the x derivative yields an equation as obtained for the standard element but with summations now over the five shape functions. Upon evaluation of these we obtain,

$$\begin{aligned} u_x = & \sum_{i=1}^{5} \varphi_i^x u_i + \frac{1}{8}\left(h + 8x + 2y\right) u_{xx} - \left(\frac{h^2}{24} + \frac{hx}{8} + \frac{x^2}{2} + \frac{xy}{4}\right) u_{xxx} \\ & - \frac{1}{16}\left(-h^2 + 4y^2\right) u_{xxy} - \frac{1}{8}\left(h^2 - 4y^2\right) u_{xyy} + \mathrm{O}(h^3). \end{aligned} \tag{3.2}$$

By setting the $\mathrm{O}(h)$ coefficient of u_{xx} to zero we obtain,

$$y = -\frac{h}{2} - 4x, \tag{3.3}$$

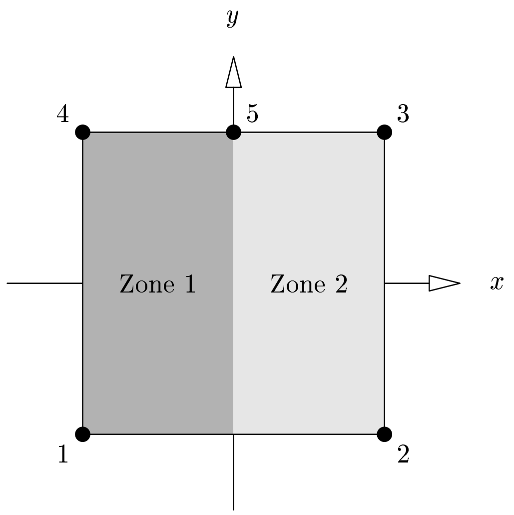

FIG. 4. Zones 1 and 2 on 1-irregular transition element with Northern irregular node.

By sampling on this line we see that the interpolant derivative is once again an $\mathrm{O}(h^2)$ approximation to u_x. Correspondingly, in zone 2 it is found that,

$$\begin{aligned} u_x &= \sum_{i=1}^{5} \varphi_i^x u_i - \frac{1}{8}(h - 8x + 2y)\, u_{xx} - \left(\frac{h^2}{24} - \frac{hx}{8} + \frac{x^2}{2} - \frac{xy}{4}\right) u_{xxx} \\ &- \frac{1}{16}\left(h^2 - 4y^2\right) u_{xxy} - \frac{1}{8}\left(h^2 - 4y^2\right) u_{xyy} + \mathrm{O}(h^3). \end{aligned} \tag{3.4}$$

which yields another line of superconvergent sampling points given by,

$$y = -\frac{h}{2} + 4x. \tag{3.5}$$

Plots of these lines are included in Figure (5). It can be seen that along the south edge of the element we have the normal single optimal point located at the midpoint. As we then sweep up the element this single point splits into two lines given by Equations (3.3) and (3.5). The two lines continue until they meet the North edge of the element. Here they meet the top of zones 1 and 2 at $(-h/4, h/2)$ and $(h/4, h/2)$ respectively. These locations are exactly at the midpoints of the upper edges of zones 1 and 2, and such a result seems to be intuitively correct as, along the North edge of the transition element we actually have two linear profiles for which we have previously noted each should have optimal sampling points at their centres. Analysis of the y derivative in zone 1 yields the following,

$$\begin{aligned} u_y &= \sum_{i=1}^{5} \varphi_i^x u_i + \frac{1}{8}(h + 2x)\, u_{xx} + y u_{yy} - \frac{1}{8}x\,(h + 2x)\, u_{xxx} \\ &- \frac{1}{16}(h + 2x)(h - 4x + 2y)\, u_{xxy} - \frac{1}{24}\left(h^2 + 12y^2\right) u_{xyy} + \mathrm{O}(h^3). \end{aligned} \tag{3.6}$$

Thus for the interpolant derivative to be an $\mathrm{O}(h^2)$ approximation to u_y the sampling point must be at $(-h/2, 0)$ in order to knock out the $\mathrm{O}(h)$ terms. In zone 2 it is found

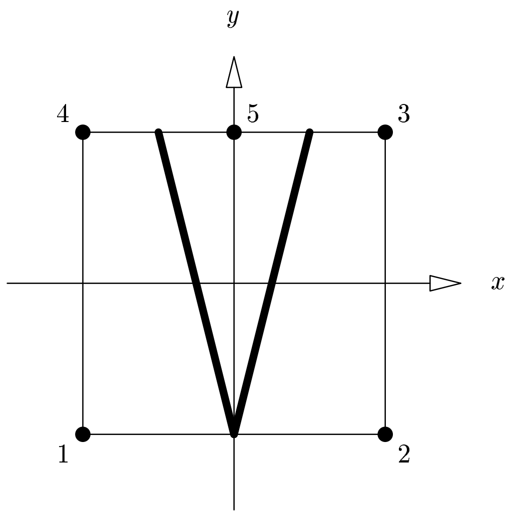

FIG. 5. Transition element superconvergent lines for the x derivative.

that,

$$u_y = \sum_{i=1}^{5} \varphi_i^x u_i - \frac{1}{8}\left(-h+2x\right) u_{xx} + y u_{yy} - \frac{1}{8} x \left(h-2x\right) u_{xxx}$$
$$- \frac{1}{16}\left(h-2x\right)\left(h+4x+2y\right) u_{xxy} - \frac{1}{24}\left(h^2+12y^2\right) u_{xyy} + \mathrm{O}(h^3). \qquad (3.7)$$

Here it can be seen that, for the interpolant derivative to be $\mathrm{O}(h^2)$ accurate, the sampling must be made at position $(h/2, 0)$. Thus the superconvergent line of the standard bilinear element has been reduced to two points upon the introduction of the Northern irregular node. If the analysis of Barlow, [3], is applied to this transition element for a class of known u, it is found that there still exists a line of high accuracy sampling points for the y derivative. A typical line for the y derivative is as detailed in Figure (6). It can be seen that the line has been affected by the presence of the irregular node. The point at which the line crosses the y-axis denoted here by an empty box can move along the axis depending upon the function u being interpolated but will always pass through the superconvergent points $(\pm h/2, 0)$ found by the Taylor series analysis and which are denoted by filled boxes. An interesting point to note here is that both of the superconvergent points found for the y derivative lie at exactly the anticipated points along the Eastern and Western edges of the element as the transition element has linear profiles along both of these edges.

C. 2-irregular Elements

The analysis will now be applied to a typical 2-irregular element. Here the configuration of the irregular nodes may either be on adjacent edges or opposite edges. In the former case, consider such an element with irregular nodes on both the North and East edges. For this element we have possibly two lines of slope discontinuity, one running between the North and South edges and the other running between the East and West edges. Consequently, we thus consider the element as having four zones instead of two as in the previous analysis. The four zones are as shown in Figure (7). By performing the

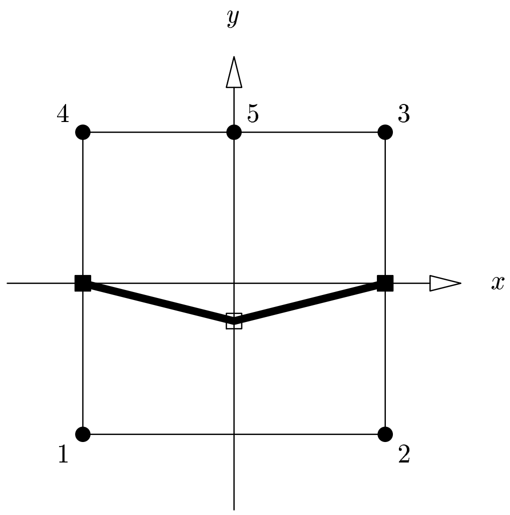

FIG. 6. 1-irregular transition element high accuracy lines for the y derivative.

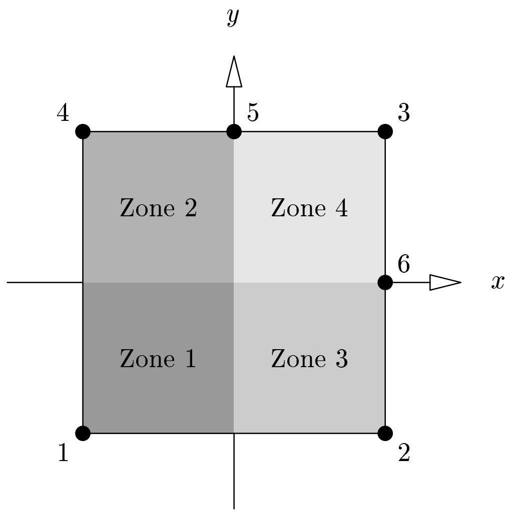

FIG. 7. Zones 1,2,3 and 4 on 2-irregular transition element with adjacent irregular nodes.

analysis as detailed in the previous cases, we obtain the results detailed in Table (I) for the approximation to the u_x derivative. It can be seen from Table (I) that, although

TABLE I. Approximation to u_x using 2-irregular transition element with adjacent irregular nodes.

Zone	Solutions of O(h) terms = 0	Resulting superconvergent point
1	$y = -\frac{h}{2} - 4x$ and $y = -\frac{h}{2}$	$\left(0, -\frac{h}{2}\right)$
2	$y = -\frac{h}{2} - 4x$ and $y = \frac{h}{2}$	$\left(-\frac{h}{4}, \frac{h}{2}\right)$
3	$y = -\frac{h}{2} + 4x$ and $y = -\frac{h}{2}$	$\left(0, -\frac{h}{2}\right)$
4	$y = -\frac{h}{2} + 4x$ and $y = \frac{h}{2}$	$\left(\frac{h}{4}, \frac{h}{2}\right)$

the familiar lines are still present in the solution of the $O(h)$ terms, there are additional terms which need to be knocked out in order to give a true $O(h^2)$ approximation to the derivative. These combine in each of the four zones to give superconvergent points as seen previously for interpolation of u_y in the 1-irregular transition element case. Inspection of the resulting points in this case yield again expected results on the edges of the element with all superconvergent points lying at the midpoints of their linear portions on the element boundary. Application of the Barlow analysis as described in [3] also yields high accuracy regions. For an example, consider the case when the function being interpolated is simply,

$$u(x, y) = x^2 + y^2. \tag{3.8}$$

Figure (8) shows the high accuracy regions on the reference element $[-1, 1] \times [-1, 1]$ which are denoted by dark lines for the derivative u_x. It can be seen from Figure (8) that the

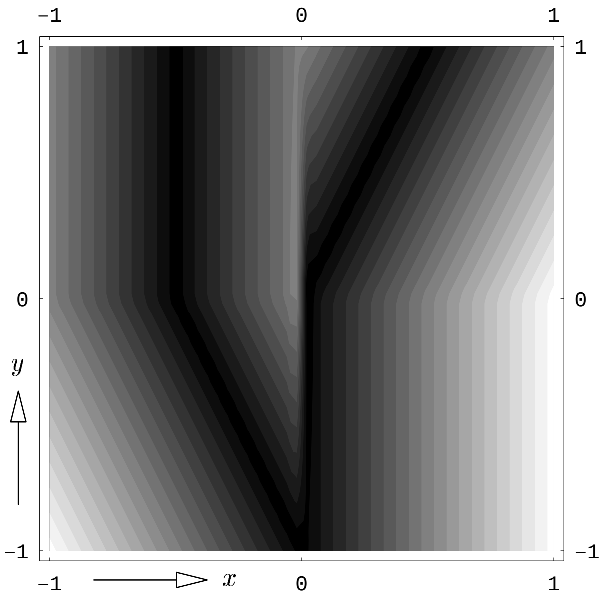

FIG. 8. High accuracy regions for interpolant to u_x for known u.

lines do in fact pass through the predicted superconvergent points of the extended Taylor series analysis. It has been observed that, for varying functions $u(x, y)$, the numerical plots of the Barlow analysis can change but the resulting lines will always pass through the aforementioned superconvergent point locations.

For the derivative u_y, the results are as detailed in Table (II) Again it can be seen that there are familiar lines which could well be expected in the case of a 1-irregular element with irregular Eastern node. In addition to these are $O(h)$ terms which force the superconvergent lines to become points as detailed in the last column of Table (II). As expected, these superconvergent points lie at the midpoints of the element boundary portions which are linear. The corresponding plots from the Barlow approach for the derivative u_y are as shown in Figure (9). It has been observed again that, for varying

TABLE II. Approximation to u_y using 2-irregular transition element with adjacent irregular nodes.

Zone	Solutions of O(h) terms = 0	Resulting superconvergent point
1	$x=-\frac{h}{2}$ and $y=-\frac{h}{8}-\frac{x}{4}$	$\left(-\frac{h}{2},0\right)$
2	$x=-\frac{h}{2}$ and $y=\frac{h}{8}+\frac{x}{4}$	$\left(-\frac{h}{2},0\right)$
3	$x=\frac{h}{2}$ and $y=-\frac{h}{8}-\frac{x}{4}$	$\left(\frac{h}{2},-\frac{h}{4}\right)$
4	$x=\frac{h}{2}$ and $y=\frac{h}{8}+\frac{x}{4}$	$\left(\frac{h}{2},\frac{h}{4}\right)$

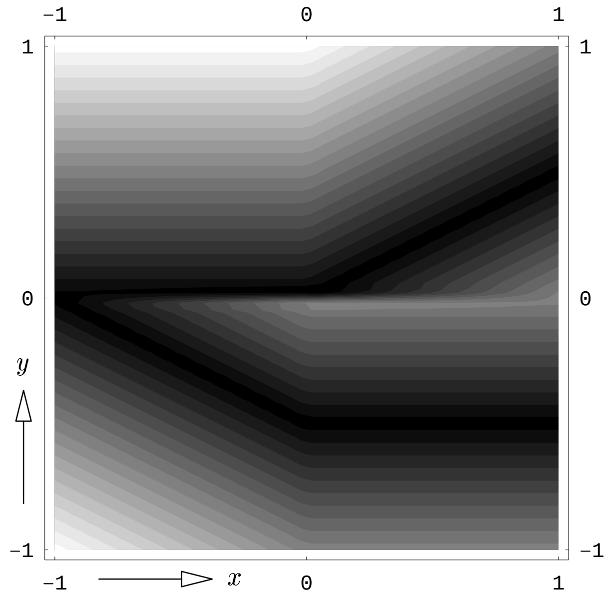

FIG. 9. High accuracy regions for interpolant to u_y for known u.

$u(x,y)$, the lines may move around but will always pass through the superconvergent points given in Table (II). It is interesting to note that there is a strong similarity between Figures (8) and (9) and the results reported by Babuška et. al. in [1] for certain mesh configurations.

There is also the 2-irregular element with opposing irregular nodes. In this case consider the element with irregular nodes on the North and South edges. In such a scenario it is necessary to split the element into only two zones as depicted in Figure (4). By doing this we effectively have two standard bilinear elements placed beside each other. The Taylor series approach then predicts that there will be superconvergent sampling lines for the derivative u_x at locations $x=\pm h/4$ on the element. Similarly for the derivative u_y there is a superconvergent sampling line running across the element at the location $y=0$. This results in superconvergent sampling points for both the interpolation of u_x and u_y existing at $(\pm h/4, 0)$. Since we effectively have two bilinear elements placed beside each other this result is as expected with a superconvergent point found to exist at the centroid of each 'element'.

D. 3-irregular Element

For this final scenario, consider a typical 3-irregular element with irregular nodes on the North, East and South edges. In this case the element will be once again split into four zones as shown in Figure (7). Results for the Taylor series analysis are shown for the derivative u_x in Table (III). These results show that for such an element, the interpolant derivative will be $\mathrm{O}(h^2)$ accurate at certain points on the boundary of the element. These points follow the now familiar pattern having locations at the midpoints of the linear portion of the element boundary upon which they reside. Application of the Barlow analysis for the interpolant to any quadratic $u(x, y)$ in both x and y confirms the locations of these points. Similar observations can be seen here as were seen in the case of the u_x derivative approximation for the 1-irregular transition element. Here though there are two lines of high accuracy as shown in Figure (10). It has been observed that, by varying a known function u, the points denoted by the empty squares are free to slide along the x-axis whilst the filled squares remain at the known superconvergent points found by using the Taylor series analysis and detailed in Table (III). For the derivative u_y we obtain results as detailed in Table (IV). Here we can see that there exist lines as were seen earlier in the analysis. Plots from the Barlow analysis can be seen in Figure (11) for the case when the known u is as described in Equation (3.8), plot (a) shows the high accuracy regions for sampling u_x and (b) for u_y. For plot (a) it is clear that the plotted lines mimic those of Figure (10). The plot also shows clearly that the

TABLE III. Approximation to u_x for 3-irregular transition element.

Zone	Solutions of $\mathrm{O}(h)$ terms $= 0$	Resulting superconvergent point
1	$\frac{1}{4}(h+4x)$ and $\frac{1}{8}(h+2y)$	$\left(-\frac{h}{4}, -\frac{h}{2}\right)$
2	$\frac{1}{4}(h+4x)$ and $-\frac{1}{8}(-h+2y)$	$\left(-\frac{h}{4}, \frac{h}{2}\right)$
3	$-\frac{1}{4}(h-4x)$ and $\frac{1}{8}(h+2y)$	$\left(\frac{h}{4}, -\frac{h}{2}\right)$
4	$-\frac{1}{4}(h-4x)$ and $-\frac{1}{8}(-h+2y)$	$\left(\frac{h}{4}, \frac{h}{2}\right)$

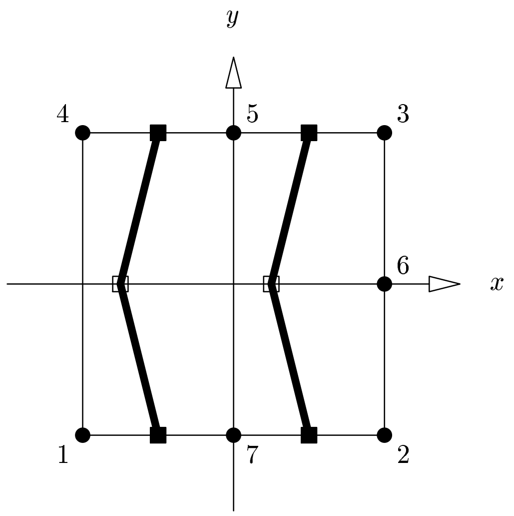

FIG. 10. 3-irregular transition element high accuracy lines for the x derivative.

TABLE IV. Approximation to u_y for 3-irregular transition element.

Zone	Solutions of O(h) terms = 0	Resulting superconvergent line
1	$\frac{1}{8}(h+2x+8y)$	$y=-\frac{h}{8}-\frac{x}{4}$
2	$-\frac{1}{8}(h+2x-8y)$	$y=\frac{h}{8}+\frac{x}{4}$
3	$\frac{1}{8}(h+2x+8y)$	$y=-\frac{h}{8}-\frac{x}{4}$
4	$-\frac{1}{8}(h+2x-8y)$	$y=\frac{h}{8}+\frac{x}{4}$

lines pass through the established superconvergent points which on the reference element $[-1,1]\times[-1,1]$ are at locations specified in Table (III) with $h=2$. Plot (b) shows that the Barlow results for this particular known u lie on the established superconvergent lines of the Taylor series for the approximation to u_y as given in Table (IV).

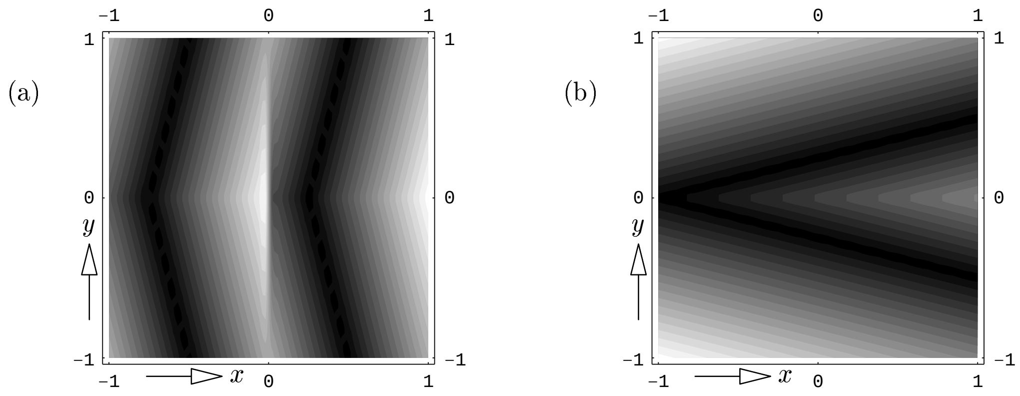

FIG. 11. High accuracy regions for interpolant, (a) to u_x and (b) to u_y for known u.

The aim of this section was to establish the locations of the sampling points for meshes containing transition elements so that a strategy could be built up for the recovery procedure of the ZZ-P error estimator. In order to have some automated set of rules it is inevitable that compromises in some areas may have to be made so that the algorithm, which rapidly becomes complicated by these considerations, does not become cumbersome and inefficient. As mentioned at the beginning of this section, it has been reported by previous researchers that for the standard quadrilateral element the optimal locations for sampling stresses (or derivatives) are at the reduced integration Gauss points. Indeed, we have demonstrated this above and have also shown this to be true for transition elements with certain node configurations. We now describe the resulting algorithms for the recovery procedure on meshes containing transition elements.

E. Element Patch Strategies for Non-Symmetric Meshes

In the previous section it was established that for the standard element the optimal sampling points lie on the reduced integration points of the element. This is in agreement with previous research findings and means that, for uniform meshes of quadrilateral elements employing bilinear shape functions, the sampling point locations for a typical element patch are clearly defined to lie at the centroids of the elements forming the patch. For the case of transition elements the findings were mixed, with some node configurations yielding optimal sampling points at the modified reduced integration points, whilst in other cases the agreement was found to be not as strong. In such cases where the agreement was less conclusive however, it is felt that sampling can still be made at the modified reduced integration points as the samples here are of a higher accuracy due to their close proximity to the optimal areas. This means that an improvement can still be expected for the recovered stresses or gradients at the nodes although there will be no guarantee of superconvergence. What now follows is the patch assembly node algorithm which will detail how the assembly nodes are determined for each node n where the stresses or gradients are to be recovered. It will be seen that sometimes the node where recovery is desired and the patch assembly node coincide but this is by no means true for all nodes. In fact the only case where the two always coincide will be for the nodes of a uniform mesh which do not lie on the boundary $\partial\Omega$ of the problem domain.

Patch Assembly Node Assignment Before proceeding it is necessary to define some terms. For a typical node n, say, the term 'surrounding nodes' means the nodes of all the elements who share n. Alternatively, the term 'neighbouring nodes' are those nodes connected to n by an element edge. Further, if node n has element count four then this means that there are four elements surrounding n and will be denoted in the algorithm as $\text{elcount}(n) = 4$. A final point to note is that any irregular mid-side node will always have element count equal to three.

This algorithm details the identification of the patch assembly node. This will be referred to as the p.a.n. during the algorithm. It is worth noting that for all nodes $n = 1, \ldots, N$, a patch assembly node must be identified.

1. For node n, compute $\text{elcount}(n)$ and store element numbers, Element1 to Element4 maximum.

2. If $\text{elcount}(n) \geq 3$ then p.a.n. $= n$.
- Stop if $n = N$ or increment n and return to Step 1.

3. Arrive here if $\text{elcount}(n)$ equals one (or two).
Count number of irregular nodes on the surrounding element(s), Element1 (and Element2).
Label as Nodes1 (and Nodes2) for the one (or two) possible surrounding element(s).

4. If $\text{elcount}(n) = 1$ and Nodes1 $= 2$ then p.a.n. $= n$.
- Stop if $n = N$ or increment n and return to Step 1.

5. Compute surrounding nodes $m = 1, \ldots, p$ for node n and $\text{elcount}(m)$ for $m = 1, \ldots, p$.

6. Loop over $m = 1, \ldots, p$. If $\text{elcount}(m) = 3$ and $m \notin \partial\Omega$ then,

  a. If $\text{elcount}(n) = 1$ then p.a.n. $= m$.
  - Stop if $n = N$ or increment n and return to Step 1.

  b. If $\text{elcount}(n) = 2$ then,

  c. If m is a neighbour of n then p.a.n. $= m$.
  - Stop if $n = N$ or increment n and return to Step 1.

7. Arrive here if there are no suitable irregular nodes in the surrounding node set.

8. Establish node r where elcount$(r) = \max(elcount(m))$ for $m = 1, \ldots, p$.

9. If elcount$(n) = 1$ then p.a.n. $= r$.
- Stop if $n = N$ or increment n and return to Step 1.

10. If elcount$(n) = 2$ then there may be more than one node with element count equal to elcount(r).

11. Select from short list the node which is a neighbour of node n. If this is node q say then p.a.n. $= q$.
- Stop if $n = N$ or increment n and return to Step 1.

The above algorithm will identify the patch assembly nodes for all nodes $n = 1, \ldots, N$. A few comments may now clarify some of the less obvious points. If the element count for node n is initially found to be three or more then the patch assembly node is trivially n itself as stated in Step 2 of the algorithm. This is due to the fact that, for the case where elcount(n)=4, the patch consists of the surrounding elements and the possibility that some of these may or may not be transition elements does not matter as samples are made on particular zones of such elements. For the case where elcount(n)=3, this means that n is an irregular node. Due to the fact that we will be sampling at the reduced integration points for the recovery scheme, two samples will come from the transition element and one from each of the other two elements. Figure (12) shows these two scenarios in parts (a) and (b) respectively. In both cases the patch assembly node is

(a)

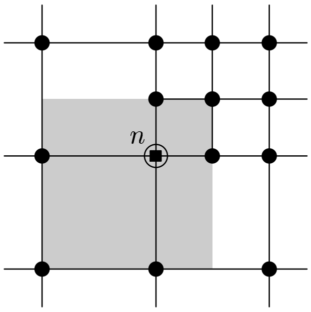

(b)

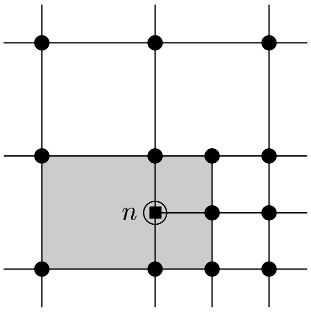

FIG. 12. Patch examples for node n where (a) elcount$(n) = 4$ and (b) elcount$(n) = 3$.

ringed, the current node n is denoted by a filled square and the patches are also shown as shaded areas for clarity. It can be seen in Figure (12) that in these two instances the patch assembly node coincides with node n. This will always be the case for elcount$(n) = 4$ and elcount$(n) = 3$ with n an irregular node.

For elcount$(n) = 1$ or elcount$(n) = 2$ the situation is different. If there is only one element surrounding node n then we have that node n is a corner node. In this case the number of irregular nodes on the element becomes important. If there is only one irregular node we proceed through the algorithm, but for the case where there are two irregular nodes we have the situation depicted in part (a) of Figure (13) and at Step 4 of the algorithm. Again the patch assembly node is node n but the patch chosen is simply the 2-irregular transition element as shown. This is due to the fact that there are four zones on such an element, as shown in Figure (7), which yield a valid sampling point each from the reduced integration points. Proceeding through the algorithm, the next situation which can arise is that the element count for node n is one and the element is a

(a) (b)

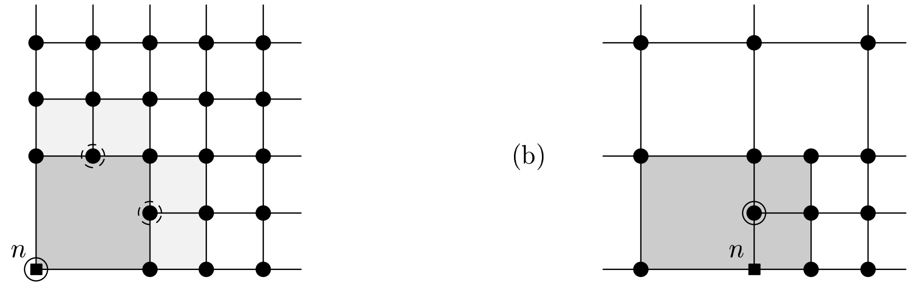

FIG. 13. Patch examples for node n where (a) elcount$(n) = 1$ with two irregular nodes and (b) elcount$(n) = 2$ with a suitable neighbour.

1-irregular element. In such a scenario the irregular node is chosen as the patch assembly node as instructed in Step 6(a) of the algorithm. This is also indicated in part (a) of Figure (13) by broken rings depending upon whether the 1-irregular corner transition element has irregular Northern or Eastern node. In addition, lighter shading is extended around both possible patch assembly nodes which will give patch configurations of the type illustrated in part (b) of Figure (12) when taken in union with the darker shaded region.

For the case depicted in part (b) of Figure (13) it can be seen that node n has element count equal to two. This means that n must also lie on the boundary of the problem domain but in this case on a side of the domain. Although at first glance this looks the same as that shown in part (b) of Figure (12) it can be seen on closer inspection that this is not the case. In this situation n is now a boundary node and the algorithm states in Step 6(c) that if any of the surrounding nodes which have element count equal to three and do not lie on the boundary are also neighbours of node n, then they are chosen as the patch assembly node. This is shown in part (b) of Figure (13) with the ringed patch assembly node lying in the domain interior as required.

We now arrive at the final steps of the algorithm. At Step 7 we have established, by a process of elimination, that there are no suitable irregular nodes in the surrounding elements which may be used as patch assembly nodes. The algorithm now embarks on establishing which node of the surrounding node set has the largest element count. If the element count for node n is one then the patch assembly node is then the surrounding node with largest element count. For the case where the mesh is locally uniform in the area of the corner node n, this means that the node diagonally opposing n with element count equal to four is chosen as the patch assembly node. This can be envisaged by imagining that, in part (a) of Figure (14), the top right element has not been refined. In this instance the patch will consist of the four corner elements all of which have same edge length. For the case where the top right element has been refined however part (a) of Figure (14) depicts exactly the choice made. It can be seen here that the node n is a corner node and the patch assembly node is again the diagonally opposing node. Although this patch choice is the same as that shown in part (a) of Figure (12) it is worth noting that in each situation the fit made to the sample points is evaluated at different positions, namely the positions of node n. A typical mesh scenario for reaching Step 10 in the algorithm can be seen in part (b) of Figure (14). Here it can be seen that none of the irregular nodes are neighbours of node n. The resulting patch assembly node is then

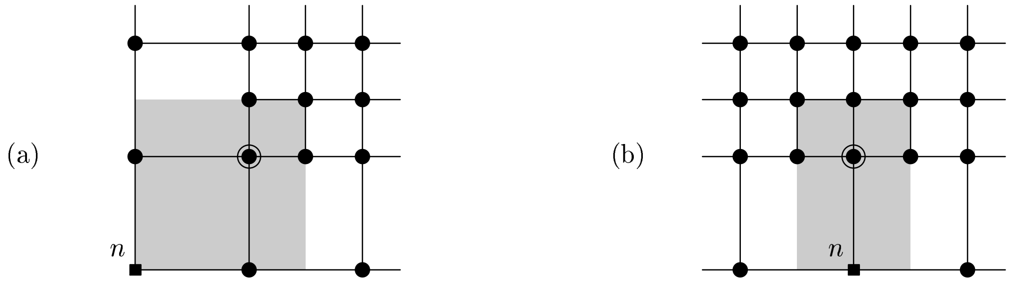

FIG. 14. Patch examples for node n where (a) elcount(n) = 1 and (b) elcount(n) = 2. Both cases have no suitable neighbouring irregular node.

chosen by finding the maximum of all element counts of the surrounding nodes as done in the previous case but this time selecting the one which is a neighbour of node n.

IV. NUMERICAL EXPERIMENTS

The error estimators are now be implemented to solve a test problem. This section should be compared with results from [9] where the error estimates have been applied to uniform meshes.

A. Spike Problem

We test the resulting adaptive algorithms using the 'spike' problem as described in [9]. To recap, this is a problem for which the displacements are all assumed to have the form,

$$\zeta(\mathbf{x}) = \frac{1}{2}\exp\left(-\alpha\left((x_1 - x_1^c)^2 + (x_2 - x_2^c)^2\right)\right),$$

where the point (x_1^c, x_2^c) lies at the centre of the plate midplane: $\Omega \equiv (0,1)\times(0,1)$. Substitution of these displacements into the equilibrium equations yields the required load to be used in the finite element model. Material properties for the plate are taken to be $E = 1$ and $\nu = 1/4$, with a plate thickness $t = 1/10$. These data yield energy and L_2-norm measures of the true solution (calculated using Mathematica, [14]) as,

$$\|\mathbf{u}\|_{E(\Omega)} \approx 3.76295844 \times 10^{-1} \quad \text{and} \quad \|\mathbf{u}\|_{L_2(\Omega)} \approx 9.90831824 \times 10^{-2}.$$

Prior to running adaptively, the computed interpolation error constants obtained using the technique described in Section (II.) for the transition element family are as given in Table (V). It can be seen in Table (V) that for the standard elements the interpolation error constants are identical to those in [9]. The transition family, however, yield differing constant values due to the irregular nodes on the element boundary and the corresponding derivative jumps. The 'Element type' column uses the element names described in Section (I.). In addition here though, is the presence of the 2_{adj}-irregular element and the 2_{opp}-irregular estimate. These are both 2-irregular elements but with the distinguishing feature that the two irregular elements lie on either adjacent element edges or opposite element edges respectively.

Adaptive results to 5% error tolerance requirement for the estimators, and with the JH-P estimator results calibrated with $\mathcal{C} = 224$ as recommended in [9], are as given in Table (VI). It can be seen that the ZZ-P estimator is performing well. This indicates

TABLE V. Computed C_1^i and C_2^i values for the transition element family for use in the plate spike problem.

Element type	Computed C_1^i	Computed C_2^i
Standard	9.404922(+1)	1.837117(+2)
1-irregular	8.668740(+1)	2.191192(+2)
2_{adj}-irregular	8.526373(+1)	2.480080(+2)
2_{opp}-irregular	6.779471(+1)	1.448804(+2)
3-irregular	6.792558(+1)	1.981567(+2)

TABLE VI. Error estimator performance for adaptive run to 5% error requirement on a mesh consisting of square elements.

ZZ-P Estimator				
I	M	$\|\mathbf{u}-\mathbf{u}_h\|_{E(\Omega)}$	θ	%error
2	245	5.473321(−1)	1.174771	65.12
4	2530	8.187460(−2)	1.214672	26.04
6	8580	2.091864(−2)	1.024459	5.69
7	15740	1.223402(−2)	1.020493	3.32
JH-P Estimator, $\mathcal{C} = 224$				
I	M	$\|\mathbf{u}-\mathbf{u}_h\|_{E(\Omega)}$	θ	%error
2	245	5.473321(−1)	0.632848	41.96
4	1565	8.187528(−2)	0.980830	21.28
6	6085	2.176806(−2)	1.020241	5.90
7	8825	1.595678(−2)	0.993295	4.21

that the sample point location and patch selection strategy developed in Section (III.) is performing as anticipated. In addition to this it can be seen that the effectivity index seems to be tending to unity, indicating that the asymptotic exactness of the estimator has been retained. The use of transition elements has been detailed previously by Choi and Park, [4]. In a second publication by Choi and Park, [5], the transition elements are implemented in a plate model along with a version of the ZZ-P estimator. However, no mention is made of the sampling points taken or indeed the patch selection procedure. It is felt that this is one of the most important areas in the implementation of this type of estimator, and it is believed that the ZZ-P implementation presented here provides information on these key areas for the first time.

Table (VI) also shows results for the calibrated JH-P estimator. It can be seen from the table that this estimator is also performing well with effectivity index close to unity. A potential area of concern, however, lies in the fact that the effectivity index is slightly less than unity meaning that the estimator is underestimating the error slightly. It is thought that this is due to the technique used to calibrate the interpolation error constants given in Table (V). This is done by scaling the interpolation error constants by the calibration constant $\mathcal{C} = 224$ which is itself found by successive uniform refinement. It may thus be argued that this calibration constant is only correct for uniform meshes and that it is not optimal to scale the transition element family interpolation error constants by the same quantity. The results for uncalibrated adaptive runs, however, seem to settle at effectivity index values of approximately $\theta \approx 225$ for true error values of 10% and smaller. This implies a calibration constant of $\mathcal{C} = 225$ which is very close to that obtained from the uniform refinement analysis of $\mathcal{C} = 224$ and used in the calibrated adaptive analysis shown in Table (VI).

Running the same problem again, but now asking for 4% error in order to compare with the ZZ-P result, and using the calibration constant found from the uncalibrated adaptive run, yields the results presented in Table (VII).

TABLE VII. JH-P estimator performance for adaptive run to 4% error requirement on a mesh consisting of square elements using calibration constant from uncalibrated adaptive analysis.

		JH-P Estimator, $\mathcal{C} = 225$		
I	M	$\Vert\mathbf{u} - \mathbf{u}_h\Vert_{E(\Omega)}$	θ	%error
2	245	5.473321(−1)	0.630036	41.81
4	1645	8.187528(−2)	0.976471	21.19
6	6725	2.123630(−2)	1.015623	5.73
7	11445	1.406744(−2)	1.013795	3.79

The convergence curves for the ZZ-P and JH-P estimators presented in Table (VI) and Table (VII) respectively can be seen in Figures (15) and (16). These curves show

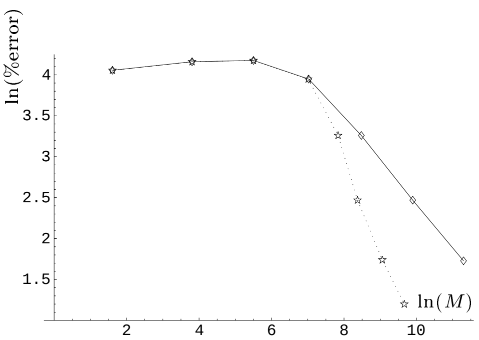

FIG. 15. Uniform and adaptive refinement convergence curves for ZZ-P estimator using square and transition elements in the plate model.

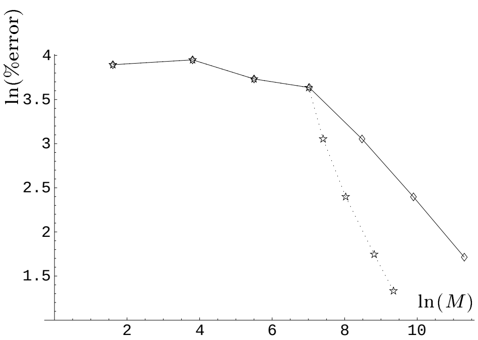

FIG. 16. Uniform and adaptive refinement convergence curves for JH-P estimator using square and transition elements in the plate model.

ln(%error) plotted against $\ln(M)$ for both uniform and adaptive refinements. In both figures, the solid line marked with diamonds denotes the uniform refinement route and the dotted line marked with stars denotes the adaptive route. It is clear from both figures that the adaptive route converges to the required tolerance quicker than the corresponding uniform refinement route as required. The meshes generated by these adaptive analyses are shown in Figure (18).

For further numerical experiments, particularly those of a comparison of the model with physical experiment data and a laminated plate, see [8].

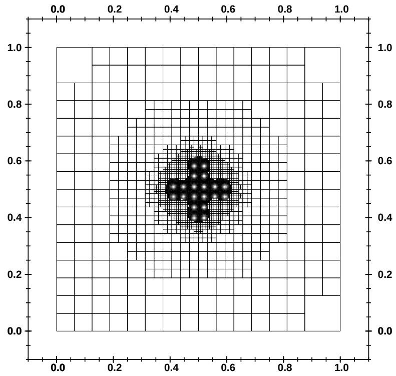

FIG. 17. Adapted square element mesh to achieve 5% error using ZZ-P estimator.

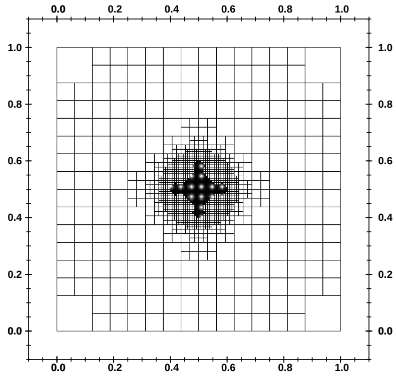

FIG. 18. Adapted square element mesh to achieve 5% error using JH-P estimator.

V. CONCLUSIONS

The above results show both the ZZ-P and JH-P estimators to be performing well. For the case of the JH-P estimator, use was once again made of the calibration constant $\mathcal{C}$ as introduced in [9]. It is thought, however, that the use of a single calibration constant could be improved by employing a set of calibration constants. In this way a calibration constant could be obtained for each of the transition element family of elements for use in adaptive analyses. These calibration constants could be obtained in the same way as the original constant $\mathcal{C}$ is for the standard element using a sequence of successively refined uniform meshes. In the case of transition elements, however, the uniform meshes should be constructed from entirely those elements for which the calibration constant is sought as detailed further in [8]. The estimator itself can also be ecxpressed as an in-plane elastic and plate elastic part as also detailed in [8]. In this way the interpolation error constants for the in-plane elastic part of the estimator become significantly smaller due to the plate thickness order in the denominator of the corresponding supremum problem being lower. Such an estimator formulation may be of use where the in-plane displacements are non-zero or where slipping may occur at the plate boundary.

As observed in [9] the ZZ-P estimate performs consistently well. When used adaptively the asymptotic exactness property often observed with this type of estimator is evident. This may be attributed to the accuracy of the sampling points used in the recovery procedure and the choice of element patches. It is felt that the main area for possible further improvement of this estimator lies in a deeper analysis of these sampling points. Although results here suggest that the chosen points are of adequate accuracy, an analysis similar to the computer based approaches of Babuška et. al. [1, 2] may yield further points and enahnce the estimator capabilities.

REFERENCES

1. Babuška, I., Strouboulis, T., Upadhyay, C.S. and Gangaraj, S.K., 'η%-superconvergence in the interior of locally refined meshes of quadrilaterals: superconvergence of the gradient in finite element solutions of Laplace's and Poisson's equations',Technical Note BN-1161 and CMC Report No. 93-09, Institute for Physical Science and Technology, University of Maryland, College Park Campus, 1994.
2. Babuška, I., Strouboulis, T., Upadhyay, C.S. and Gangaraj, S.K., 'Computer-based proof of the existence of superconvergence points in the finite element method; superconvergence of the derivatives in finite element solutions of Laplace's, Poisson's and the elasticity equations', *Numerical Methods for Partial Differential Equations*, **12**, pp.347-392, 1996.
3. Barlow, J., 'Optimal stress locations in finite element models', *International Journal for Numerical Methods in Engineering*, **10**, pp.243-251, 1976.
4. Choi, C. and Park, Y., 'Transition plate-bending elements for compatible mesh gradation', *Journal of Engineering Mechanics*, **118**, pp.462-480, 1992.
5. Choi, C. and Park, Y., 'An adaptive h-refinement using transition element for plate bending problems', *International Journal for Numerical Methods in Engineering*, **35**, pp.145-163, 1992.
6. Gupta, A.K., 'A finite element for transition from a fine to a coarse grid', *International Journal for Numerical Methods in Engineering*, **12**, pp.35-45, 1978.
7. Johnson, C. and Hansbo, P., 'Adaptive finite element methods in computational mechanics', *Computer Methods in Applied Mechanics and Engineering*, **101**, pp.143-181, 1992.
8. Ludwig, M.J., 'Finite element error estimation and adaptivity for problems of elasticity', Ph.D. Thesis, Department of Mathematical Sciences, Brunel University, Uxbridge, England, 1998 (see `www.brunel.ac.uk/~icsrbicm/tech_rep.html#99`).
9. Ludwig, M.J., Shaw S. and Whiteman, J.R., 'Adaptive numerical solution of thick plates using first-order shear deformation theory. Part I: Error estimates.', BICOM Technical Report 00/06 (see `www.brunel.ac.uk/~icsrbicm/tech_rep.html#00`). Submitted to Numer. Meth. Part. Diff. Eqns.
10. Mackinnon, R.J. and Carey, G.F., 'Superconvergent derivatives: a Taylor series analysis', *International Journal for Numerical Methods in Engineering*, **28**, pp.489-509, 1989.
11. Ochoa, O.O. and Reddy, J.N., *Finite Element Analysis of Composite Laminates*, Kluwer Academic Publishers, Dordrecht, The Netherlands, 1992.
12. Reddy, J.N., *Energy and Variational Methods in Applied Mechanics*, John Wiley & Sons, New York, 1984.
13. Reddy, J.N. and Miravete, A., *Practical Analysis of Composite Laminates*, CRC Press, Florida, 1995.
14. Wolfram, S., *Mathematica: A System for Doing Mathematics by Computer*, Addison-Wesley Publishing Company, Inc., 1991.
15. Zienkiewicz, O.C. and Zhu, J.Z.,'The superconvergent patch recovery and *a posteriori* error estimates. Part 1: The recovery technique', *International Journal for Numerical Methods in Engineering*, **33**, pp.1331-1364, 1992.
16. Zienkiewicz, O.C. and Zhu, J.Z.,'The superconvergent patch recovery and *a posteriori* error estimates. Part 2: Error estimates and adaptivity', *International Journal for Numerical Methods in Engineering*, **33**, pp.1365-1382, 1992.